Scanning-less wide-field single-photon counting device for fluorescence intensity, lifetime and time-resolved anisotropy imaging microscopy

Jean-Alexis Spitz, Ryohei Yasukuni, Nicolas Sandeau, Minako Takano, Jean-Jacques Vachon, R. Méallet-Renault, Robert Bernard Pansu

Wide-field single photon counting device for fluorescence intensity, lifetime and time-resolved anisotropy imaging microscopy.

J.-A. SPITZ[1,2,*], R. YASUKUNI[1], N. SANDEAU[3], M TAKANO[1], J.-J. VACHON[1], R. MEALLET-RENAULT[1] & R.B. PANSU[1,*]

1 -PPSM, Institut d'Alembert, ENS Cachan, CNRS, UniverSud, 61 av President Wilson, F-94230 CACHAN, France

2 - LBPA, Institut d'Alembert, ENS Cachan, CNRS, UniverSud, 61 av President Wilson, F-94230 CACHAN, France

3 - LPQM, Institut d'Alembert, ENS Cachan, CNRS, UniverSud, 61 av President Wilson, F-94230 CACHAN, France

Correspondence to: Dr. Robert B. Pansu. Tel: + 33 1 47 40 27 19; Fax: + 33 1 47 40 24 54; e-mail: pansu@ppsm.ens-cachan.fr

Key words: Fluorescence, anisotropy, FLIM, tr-FAIM, single photon counting, Quadrant anode, wide-field imaging

Summary

A single photon counting system for FLIM and fluorescence anisotropy wide-field imaging is described and characterized in this paper. The two polarizations of the fluorescence are divided by a Glan prism and acquired at the same time by the Q_A detector. Fluorescence

decay profiles can be reconstructed for any desired area up to each pixel and used to calculate time resolved fluorescence anisotropy decays.

Introduction

Biological and physical sciences have an increasing interest in fluorescence spectroscopy imaging. Fluorescence emission can give access to different parameters such as intensity but also lifetime and anisotropy (Lakowicz 1999; Valeur 2001). Indeed, the spectroscopy of fluorescence is a powerful tool to probe viscosity, structural change, functional information and more generally speaking to probe local environment (Fleming 1986).

Ion indicators where the fluorescence lifetime depends on the chelation state have been found and are used to measure calcium concentration (Schoutteten *et al.* 1999). FLIM is also used to measure protein contact and deformation through FRET (Förster 1959). Indeed, the presence of an absorbing dye within a few nanometers of the fluorescent protein induces a reduction of the fluorescence lifetime (Millar 1996). The early application of the principle has been the building of Cameleon, a construction that uses intramolecular FRET to measure Ca (Miyawaki *et al.* 1997). Anisotropy is a parameter that is used for more general puposes. It measures the randomization of direction of the transition dipole of the emitter. Most of the time this randomization is due to the rotational dynamics of the fluorescent label, however it can also be due to the energy transfer in a FRET process (Tramier *et al.* 2000). Quite often a change in the movement of the fluorescent label can be predicted or expected when a biological event occurs and it can be used to measure protein dimerization through FRET between identical labels (Homo FRET) (Gautier *et al.* 2001).

There are three main FLIM techniques: phase fluorimetry, time gated set-ups and single photon counting systems (SPCS) (Herman *et al.* 1999). The first two are widely used due to the development of CCD cameras (Wang *et al.* 1992; Gadella *et al.* 1993; So *et al.* 1995; So *et al.* 1998). Although, the latter remains more unconventional, it seems more respectful to the sample because of its increased sensitivity. In the most common SPCS FLIM set-ups (Buurman *et al.* 1992), the laser scans the image pixel by pixel which slows down the acquisition process. The use of wide-field imaging detectors for full parallel pixel acquisition has not been extensively developed (Emiliani *et al.* 2003). Moreover, instead of sampling the detection, which significantly reduces the sensibility, each emitted photon is taken into account.

Furthermore, time resolved fluorescence anisotropy imaging has been described. Jovin *et al.* developed a technology in which the phase delay and intensity ratios between the polarized components of the fluorescence signal are recorded, leading to estimations of rotational correlation times and limiting anisotropies. This set-up was successfully applied to rotational dynamics studies in solution and emFRET in bacteria expressing EGFP (Clayton *et al.* 2002). However, in their experiments, the two different polarizations are acquired successively. French *et al.* are able to image the rotational motility of a fluorophore thanks to a time gated fluorescence lifetime imaging system (Siegel *et al.* 2003). Time resolved fluorescence anisotropy has also been successfully applied to single molecule spectroscopy (Ha *et al.* 1999; Schaffer *et al.* 1999).

In our set-up, the whole decay profile of the two polarizations is acquired simultaneously with a single photon counting system. Thus, there is no sampling of the fluorescence decay. Moreover, the two polarizations are acquired at the same time, with the same sample, at the same position, with the same experimental conditions preventing us from artefacts such as instrument drift, evolution of the sample or photobleaching.

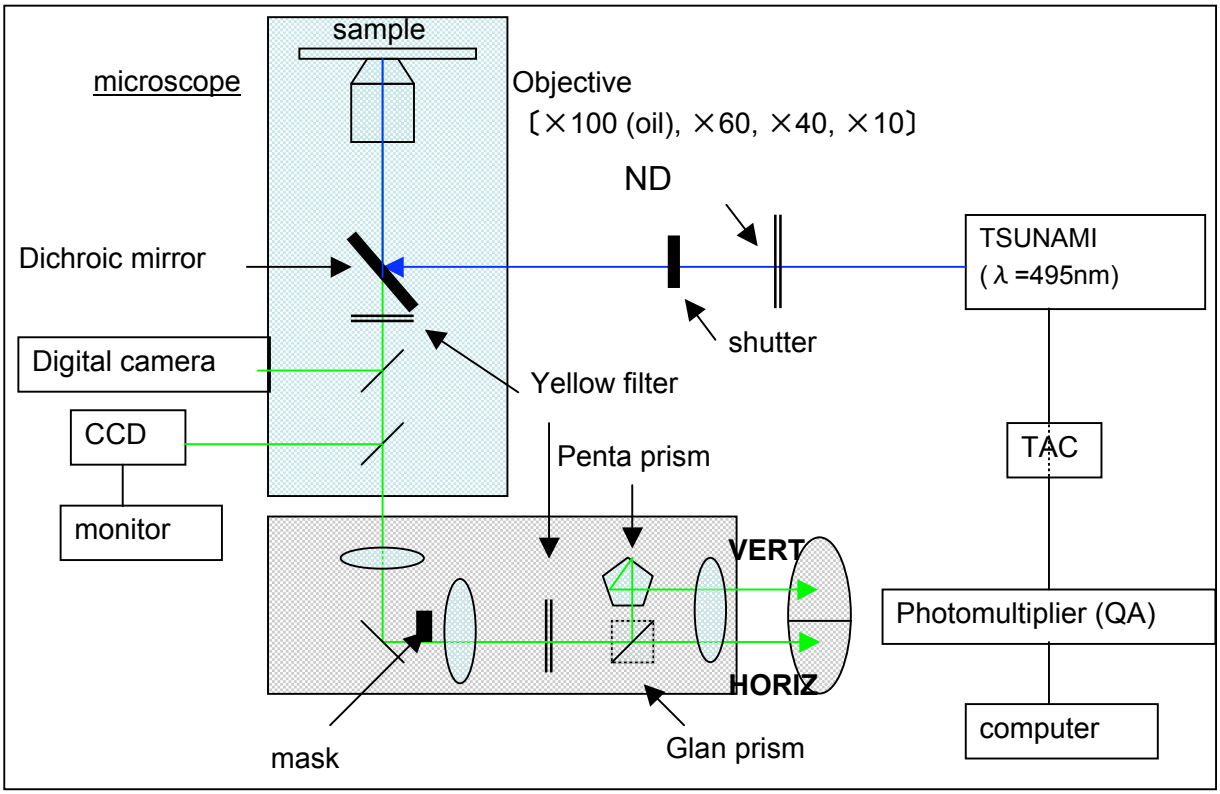

Figure 1

Materials and methods

The experimental device is shown on Fig. 1. The excitation source is an argon-ion laser pumped mode-locked Ti/sapphire laser (Tsunami by Spectra-Physics). Its output is repetition-lowered by a pulse-picker and frequency doubled in a BBO crystal to produce a 1.2 ps excitation source operating at a 4 MHz repetition rate, and which can be tuned from 430 to 500 nm. The laser beam enters the Nikon 2000 TE inverted microscope, being reflected toward the sample by the dichroic beamsplitter. The laser is focused on the back focal point of the objective and goes through the sample as a parallel beam, thus providing a wide-field excitation of the sample.

Figure 2

The fluorescence generated in the sample is guided to a time-resolved single-photon-counting photo-multiplier (Q_A) from Europhoton Gmbh (Berlin http://www.europhoton.de/). During this process, half of the image is cut by a mask. The other half reaches a 45° removable Glan prism which divides the fluorescence into the horizontal (transmitted) and vertical (reflected) polarization components. The vertical polarization is then flipped and redirected by a pentaprism (Fig. 2). At the end of the line, the sensible surface of the detector receives a composite image comprising two spatially identical and symmetrical images of the sample that differ in their polarization content.

Q_A is a multi-channel plate photo-multiplier (PM) working in the single photon counting mode. The anode is composed of five conductive parts. When a photoelectron is produced, an avalanche is created in the two multichannel plates and spreads over the five anodes. The position of the photon on the photocathode can be calculated from a weighted mean of the five charges collected on the anodes. For each photon detected, five values are measured and saved on a hard disk: the delay between the laser pulse and the arrival of the photon on the PM, the absolute arrival time (i.e. the time from the beginning of the measurement), the X and Y position of the photon on the photocathode and the total avalanche amplitude. The histogram of the number of photons collected per pixel gives the intensity image of the sample. The histogram of the number of photons collected as a function of absolute arrival time gives the evolution of the global fluorescence intensity and provides a

way to monitor photobleaching. The histogram of the total number of photons as a function of the delay between the laser pulse and the fluorescence gives the global fluorescence decay of the sample. Some kinds of histograms can also be constructed for selected areas of the image, thus giving the specific fluorescence decay of the selected area. For each pixel we also calculate the sum of all the delays between the laser pulse and the collected photons. When divided by the number of photons arrived on each pixel this sum of all the delays gives the average fluorescence lifetime as a FLIM image. This is a fast and robust way to make FLIM images.

The time resolved anisotropy function, r(t), is then calculated (without deconvolution of the instrument response function) from the Perrin equation :

$$r(t) = \frac{I_{//} - GI_{\perp}}{I_{//} + 2GI_{\perp}} \qquad (1)$$

where G is the apparatus function (Cf. supra) and $I_{\perp}$ and $I_{//}$ are the perpendicular and parallel components of the fluorescence polarization.

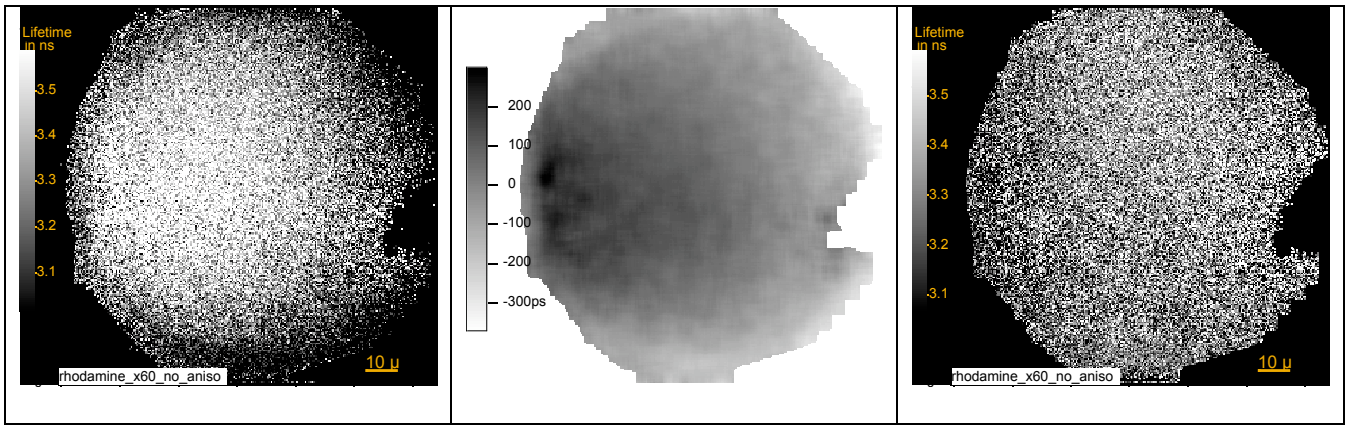

Figure 3

Results and discussion

We present here the different aspects of the set-up characterization. First, we shall focus on the fluorescence lifetime and intensity measurements. Then, we will characterize the space resolution of this new detector. Finally we will discuss the measurement and imaging of fluorescence anisotropy.

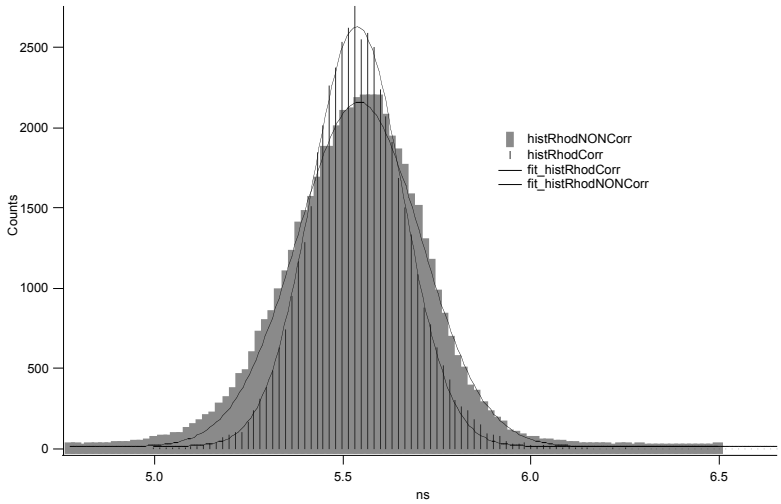

Fig. 4: Histogram of the collected photon vs. lifetime before and after correction of time transit

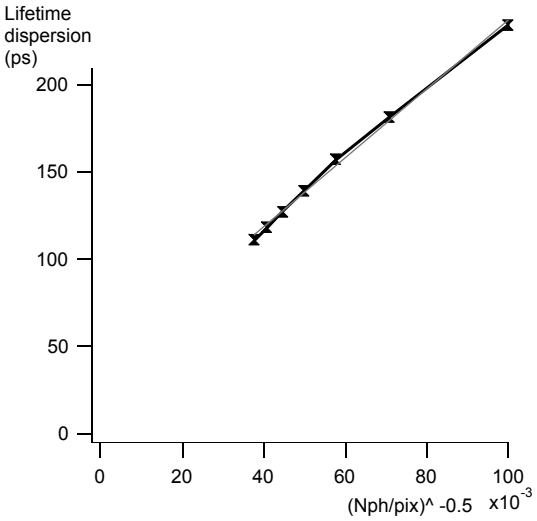

Fig. 5: Evolution of the lifetime dispersion with the number of photon per pixel. The pixels of an image of a rhodamine sample were sorted according their intensity and the lifetime distribution was fitted with a Gaussian whose width is the lifetime dispersion.

Time measurement

Lifetime measurement correction.

The crude FLIM image of a homogeneous sample (Rhodamine 6G (Magde *et al.* 2002), 10^{-4} M in water) is shown on Fig. 3a. It shows a lifetime between 3 ns (black pixel) and 3.6 ns (white pixel), with more white pixels in the middle of the image. This homogeneous sample should show a sharp distribution in fluorescence lifetime. Thus, when the center of the image

seems to have a longer lifetime, the periphery shows a shorter one. The artificial delays, that are observed, are due to electronics. Indeed for each avalanche, the propagation time of the induced current pulse through the multichannel plate to reach the discriminator depends on the location of the avalanche. To correct those constant time transit variations, we use a time transit correction map. To build up this map, we use a rhodamine sample in water that has a homogeneous life time on the whole sample and can be thus used as a reference. We calculate the difference between the time measured on each pixel and the average value, which is the expected lifetime; this difference will then be automatically subtracted to all future FLIM images.

Dispersion of the average fluorescence time.

If we look at Fig. 3c, we see a uniform value for the measure of fluorescence lifetime, but a remaining dispersion (Fig. 4). We shall show that this residual dispersion is due to photon statistics.

The precision of average fluorescence time measurements depends upon the number of photons collected by each pixel of the image. In the case of a monoexponential decay (e.g. rhodamine), the distribution P(t) of the photon arrival time is k.exp(-kt) were 1/k is the fluorescence lifetime. The expected value of the mean arrival time of N photons is 1/k and the variance of these arrivals times is 1/k_. The variance of the mean arrival time of N photons will be $1/(k?N)$. This variance will tend to zero as N approches infinity. Thus, the number of photon per pixels has been counted and an average fluorescence time distribution has been build according to this number of photon per pixels. We get a family of Gaussians whose widths give the lifetime dispersion as a function of the number of photons (Fig. 5). The width scales linearly with $1/\sqrt{N}$ and extrapolates to 39 ps. This shows that the dispersion of

fluorescence time is due to photon statistics and the extrapolated value to infinite photon count gives the quality of the correction by the transit time map.

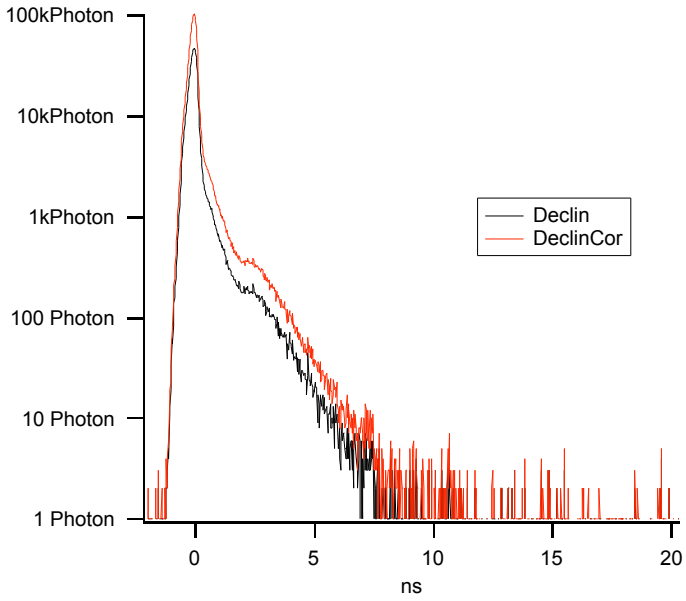

Fig.6: Pulse and corrected pulse.

Temporal resolution

The temporal resolution of the set-up is limited by our detector. To determine it, we use a 1.2 ps pulse and measure the time response of our detector (Fig. 6). The middle height width of the recorded pulse is around 310 ps. This is the shortest event we can efficiently measure and it gives us an idea of our temporal resolution. Global fluorescence decays can also be corrected from the transit time deviation. After this correction, the full width at half maximum of the pulse reaches the value of 150 ps. It can be reduced to 130 ps only if the center of the detector is used. This time resolution agrees with the one expected from the diameter of the holes in the MCPs.

Time shift from the microscope objectives

The use of 4 different objectives leads to another small time shift from one objective to another because, though objectives are designed to perform with same work distance, the lenses sizes are different. This explains why the way through the x40 is shorter than the other (- 75 ps) whereas the x100 induces an extra time of 65 ps. Again, those shifts are automatically corrected to set all pulses at the same point.

Intensity measurements

Gain correction

Some areas of our detector can present different gains. The lighting of the sample may also affect the intensity image because some areas might be more lighted than others. As previousy mentioned, a software correction is necessary to supplement these sensibility variations (Fig. 7). The gain factor map is calculated from a rhodamine in aqueous sample.

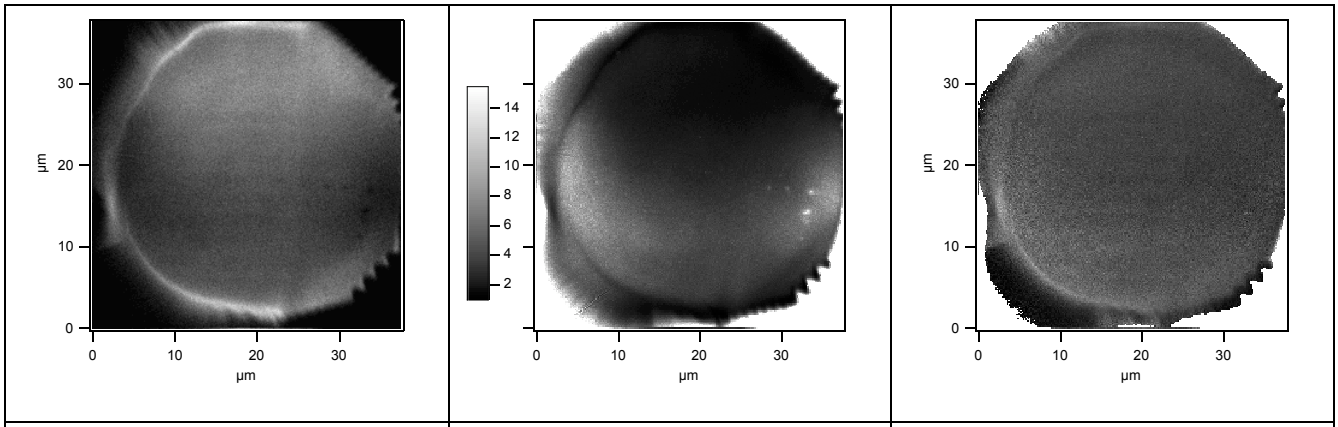

Fig. 7: Gain correction. a) Crude image of a rhodamine in basic water sample. b) Gain factor correction map calculated from another sample. c) Corrected image of the first sample using the gain factor correction map.

N.B.: On the right part of the uncorrected image (Fig. 7a), we can notice small dark spots which are areas of the detector that are less sensible than the average.

N.B. 2: The overload on the periphery of the image is not due to reflections on the inner walls of our set-up neither to accumulation of miscalculated photons thanks to the help of the fifth surrounding anode (Fig. 8).

Dead time

Once a photon reaches the anode, it has to be proceeded by the set-up. During this dead-time, any other photon will not be taken into account. This dead-time is determined by sorting the acquired photons according to their delay relative to the previous photon (Fig. 9). Thus, we measure a dead time of 2.15 µs.

Saturation

The histogram (data not shown) of the amplitude of avalanches is independent of count rate. Thus the saturation of the count rate is not due to a saturation of the MPC channel. The saturation due to the 2.15 µs dead time of the charge amplifiers should be 465 kHz. The measured saturation rate of 72 kHz (Fig. 10) might be due to the data transfer later in the process.

Spatial resolution

The determination of the spatial resolution of the device was carried out by imaging isolated fluorescent nanolatex. These latexes, from Molecular Probes (F-8787), have a diameter of 20 nm, which is below the resolution. The size of the smallest spots gives us the spatial resolution. The latexes are spin-coated on a microscope slide after dissolution (0.2% in mass) in a 1% PolyVinyl Alcohol aqueous solution according to the protocol described by R. Méallet-Renault *et al.* (Méallet-Renault *et al.* 2000). (1) 5 s 300 rpm, 2) 1 min 1600 rpm)

Thanks to a piezoelectric plate, a series of images are recorded at different heights above and under the focus plan. (Fig. 11)

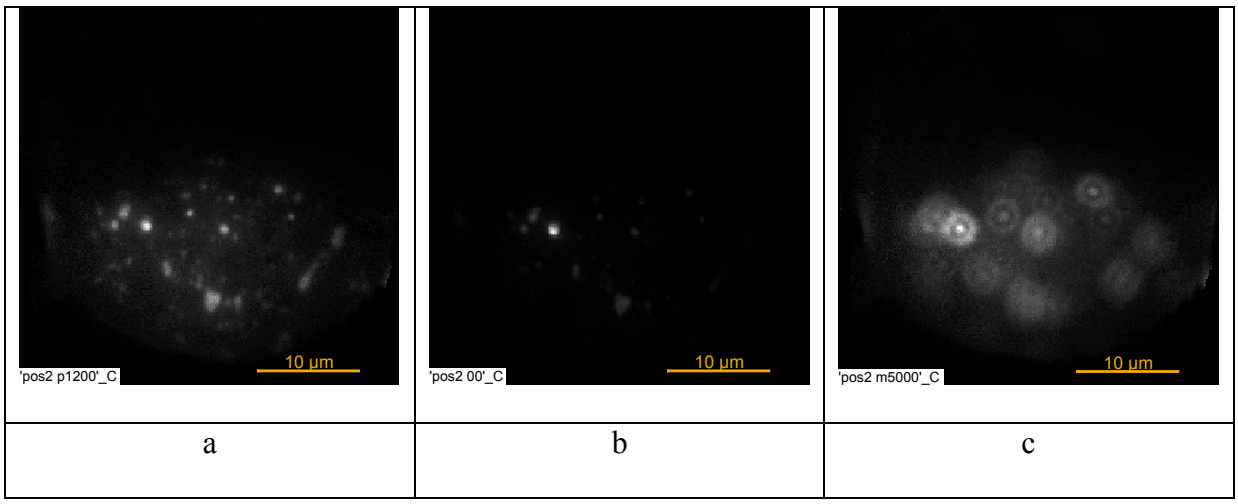

Figure 11 :Images of spin-coated 20-nm f luorescent nanolatex in PVA film. (b) is the image in focal plane, (a) is the image 1.2 µm underneath and (c) is the image 5 µm over the focal plane.

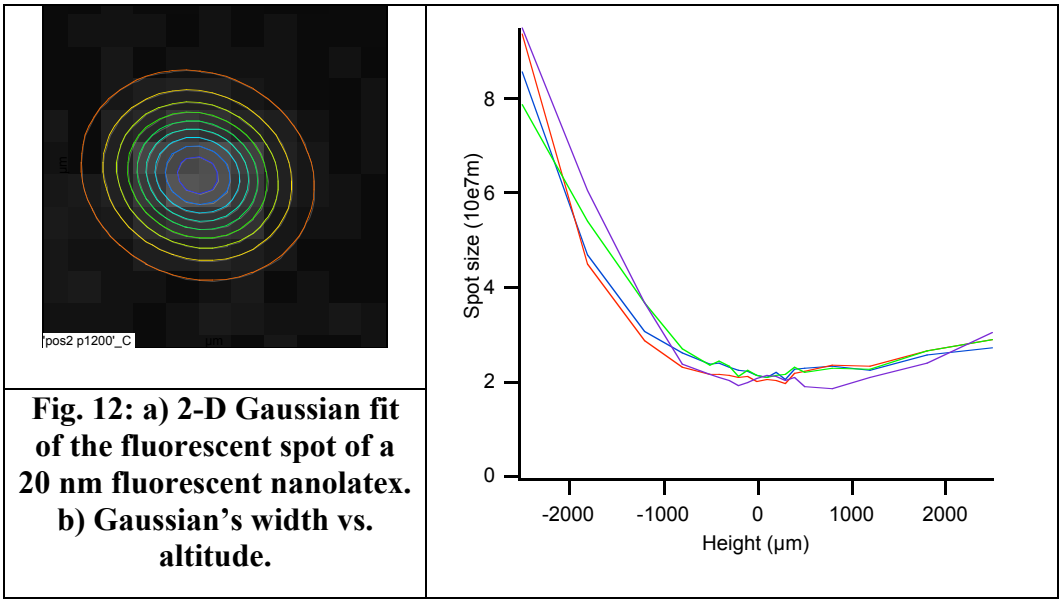

Fig. 12: a) 2-D Gaussian fit of the fluorescent spot of a 20 nm fluorescent nanolatex. b) Gaussian's width vs. altitude.

The smallest fluorescent marks, corresponding to isolated nanolatex particle, are fitted by a series of 2-dimension Gaussians whose widths are plotted in a function of the altitude on Fig. 12. The lowest point of the resultant curve corresponds to the focus plan and the size of the spot (200 nm) is the spatial resolution of the imager. The Gaussian half-width of 200 nm corresponds to an Airy radius of 400 nm. The pixel size is smaller than the resolution limit and does not limit the overall spatial resolution of the set-up.

NB: The dissymmetry of the curve Fig. 12-b is due to the imperfectly corrected spherical aberration of our set-up.

Anisotropy

Delay due to the set-up

The two different polarizations of the emitted fluorescence have different courses through the set-up. Indeed, the vertical component is reflected by the Glan prism and then by the pentaprism. Consequently, the optical path way of this polarization is longer than the other, leading to an extra delay of 160 ps (4,8 cm Fig. 13). Before any calculations on these decays, such as anisotropy calculation, this shift is corrected by computer post-treatment. A typical corrected FLIM image of the two polarizations of rubrene fluorescence is presented on Fig. 14. No deconvolution is necessary because fluorophores used in this study have long fluorescent lifetimes.

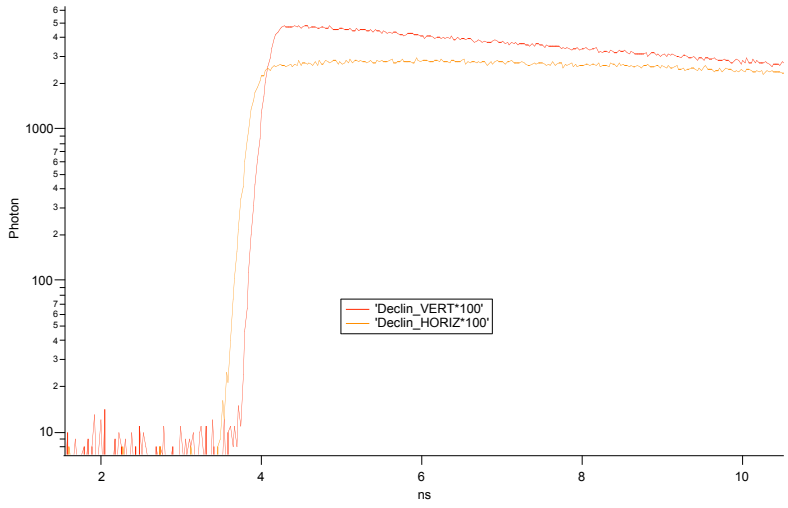

Fig. 14: Parallel and perpendicular decays of rubrene fluorescence. Fluorescence decays of rubrene in solution in squalane, before correction of the pathway shift.

Effect of the collection angles

Since we intend to use different scales of sample, we use different microscope objectives (x10, x20, x40, x60 and x100). Those objectives have different numerical aperture (resp. 0.3, 0.45, 0.6, 0.95 and 1.45). It is well known that measured anisotropies depend on the collection angle. For high collection angles, we start to collect the light emitted by the x-oriented population. Thus the observed anisotropy is reduced. This collection angle (u) is a function of the numerical aperture of the objective and of the refractive index in the fluorescent solution (n'). $\sin u = \frac{NA}{n'}$ (2)

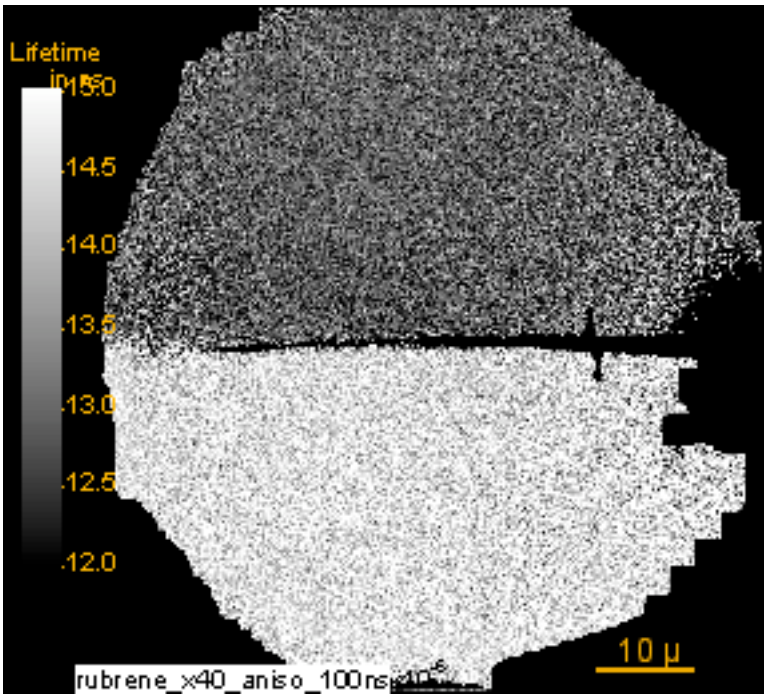

i. B - Effect of the numerical aperture of the objectives

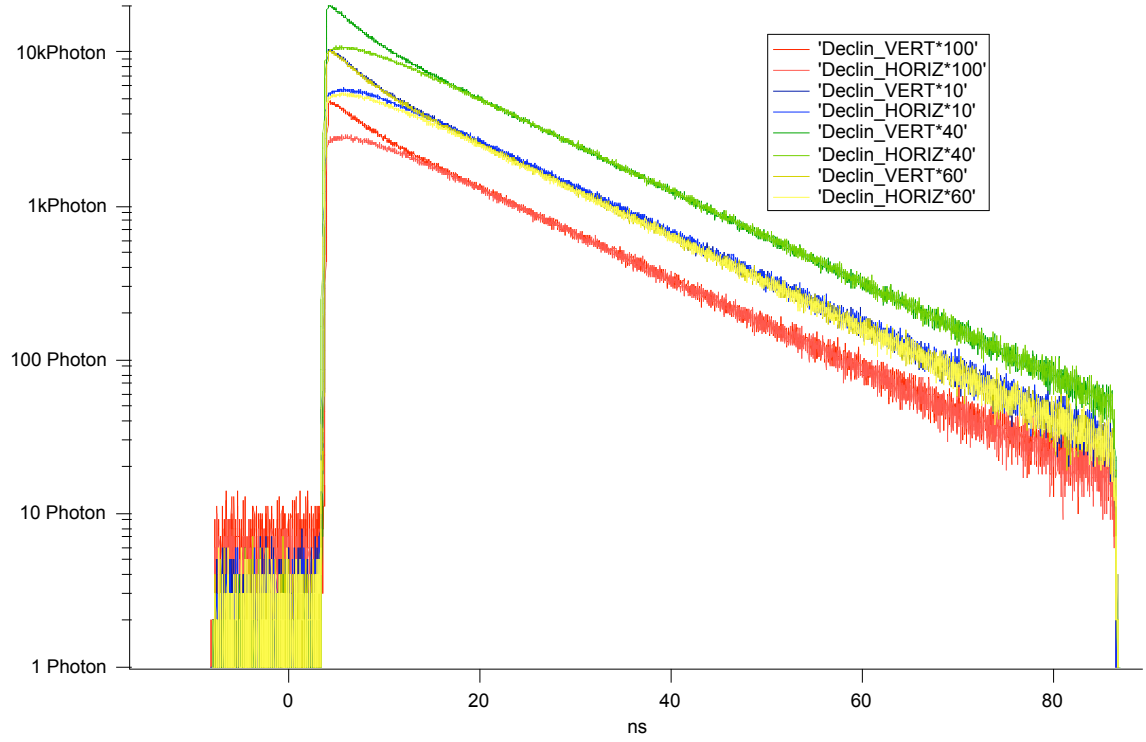

Fig. 15: Fluorescence decays of rubrene in squalane. The decays have been recorded using 4 different microscope objectives and numerical apertures. The decay for parallel polarization (resp. perpendicular) has been calculated from the upper part (resp. bottom part) of the image.

We have studied the effect of the depolarization of the anisotropy of a solution of rubrene in squalane (n'=1,4474 (Tripathi 2005)) with these increasing collection angles. (Fig. 15, 16 and Table 1). The anisotropy measured in cuvette within a calibrated spectrofluorimeter has been added with a Numerical Aperture of 0. The predicted anisotropy value has been calculated by a full-vectorial modeling which is based on a method proposed by Enderlein (Enderlein 2000). The method permits the calculation of the electric field (**Ei)** (in the image space) emitted by a fluorophore (i) in the object space. It depends on the position and the orientation of the emitting dipole. The index of the fluorescent solution, the polarization of the excitation beam and the characteristics of the microscopes (NA, magnification) and of the fluorophores are taken into account too. In this case, the emitted field is projected along the two

perpendicular directions of polarization (one is parallel to the polarization excitation beam).

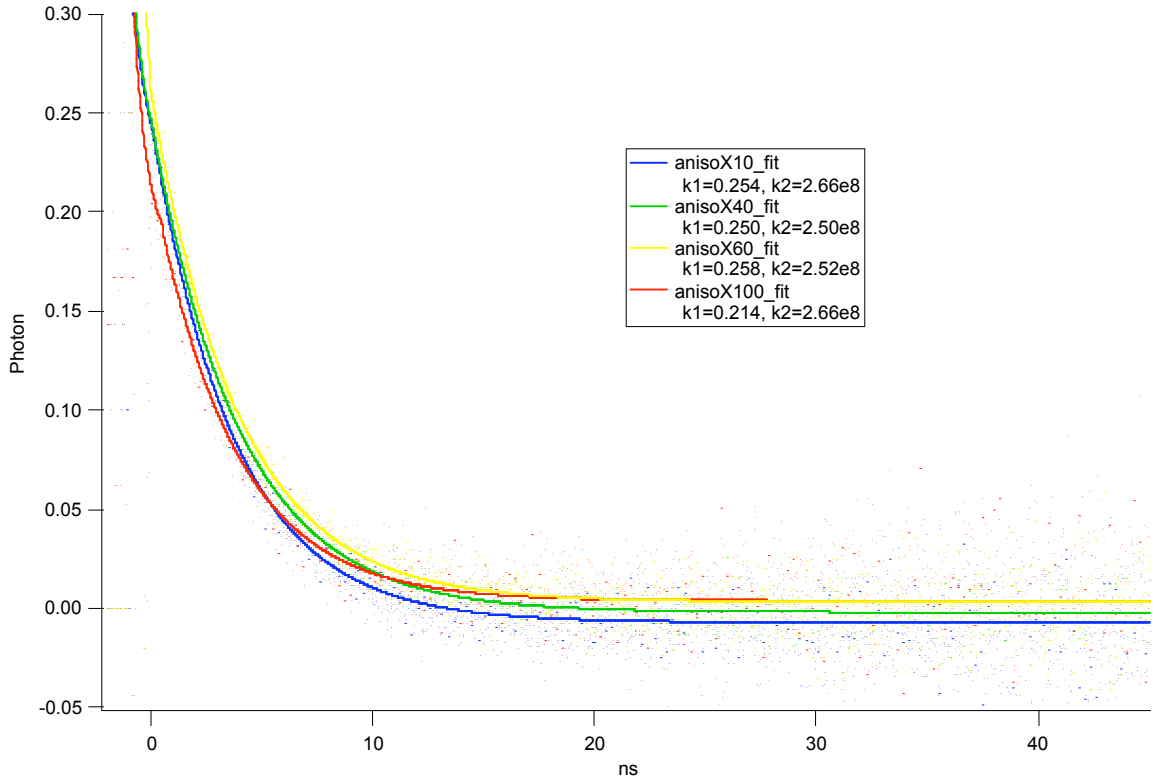

Figure 16
Time-resolved anisotropy of rubrene in squalane with different numerical apertures. The anisotropy has been calculated according to the Eq. 1 from the decays recorded using 4 dif ferent microscope objectives.

Therefore in the focal plane of detection, we can calculate two intensity values ($Ii_{//}=\|\mathbf{Ei}_{//}\|^2$ and $Ii_{\perp}=\|\mathbf{Ei}_{\perp}\|^2$) corresponding to the two analysis directions of polarization. Fluorescent objects are spatially incoherent, thus the intensity on the photo-detector is equal to the sum of all intensities emitted by each fluorophore of the solution. In this case and to take into account the randomly orientation of fluorophores, we have integrated the two intensity values ($Ii_{//}$ and $Ii_{\perp}$) on all possible orientations (3 angles) and on the volume (3 directions) of the object. One can note that three angles are necessary to describe completely the orientation of the fluorophore with its absorption dipole which is not collinear to the emission dipole. Therefore we can calculate the anisotropy from the two intensity values ($I_{//}$ and $I_{\perp}$) resulting of the two triple integrals for different fluorophores and different microscope objectives. The predicted decrease of anisotropy (Axelrod 1979) is observed as previously stated with a different

configuration (Schoutteten *et al.* 1997) but does not prevent anisotropy measurement up to a collection angle of 50° where it can be neglected as reported by Seigel *et al* (Siegel, Suhling *et al.* 2003).

The time evolution of polarized fluorescence intensity is of two types $I_{//}$ and $I_{\perp}$ (Fleming 1986)

$$I_{//} = I_0 \exp(-\frac{t}{\tau_{rot}})(1 + 2r(t)) \qquad (3)$$

$$I_{\perp} = I_0 \exp(-\frac{t}{\tau_{rot}})(1 - r(t)) \qquad (4)$$

When high collection angles are used, the collected intensity with a vertical (resp. horizontal) analyzer is a linear combination of $I_{//}$ and $I_{\perp}$. Thus, the characteristic rotational correlation times are not affected by the collection angle used.

Anisotropy in thin films

Measurements of anisotropy in films will depend also on the collection angle but with different relations since the radiation pattern is no longer toroidal. Spin-coated 50-nm films of a fluorescent dye (PM567 30 µg.g^{-1} in 10 % PMMA in toluene, 1) 10 s 1000 rpm, 2) 50 s 3000 rpm) have been studied with the different objectives (Fig. 17). The relaxation of the anisotropy observed in such a film is not due to the Brownian motion of the excited state in the polymer film but to the Förster resonance energy transfer (FRET) from the excited molecule to one of its neighbour. The angular distribution of the transition moment after one FRET jump can be calculated. For a given distance R the jump probability is proportional to

$$\kappa^2 = \left[3(\vec{u}.\vec{p}_0)(\vec{u}.\vec{p}_1) - (\vec{p}_0.\vec{p}_1)\right]^2 \qquad (5).$$

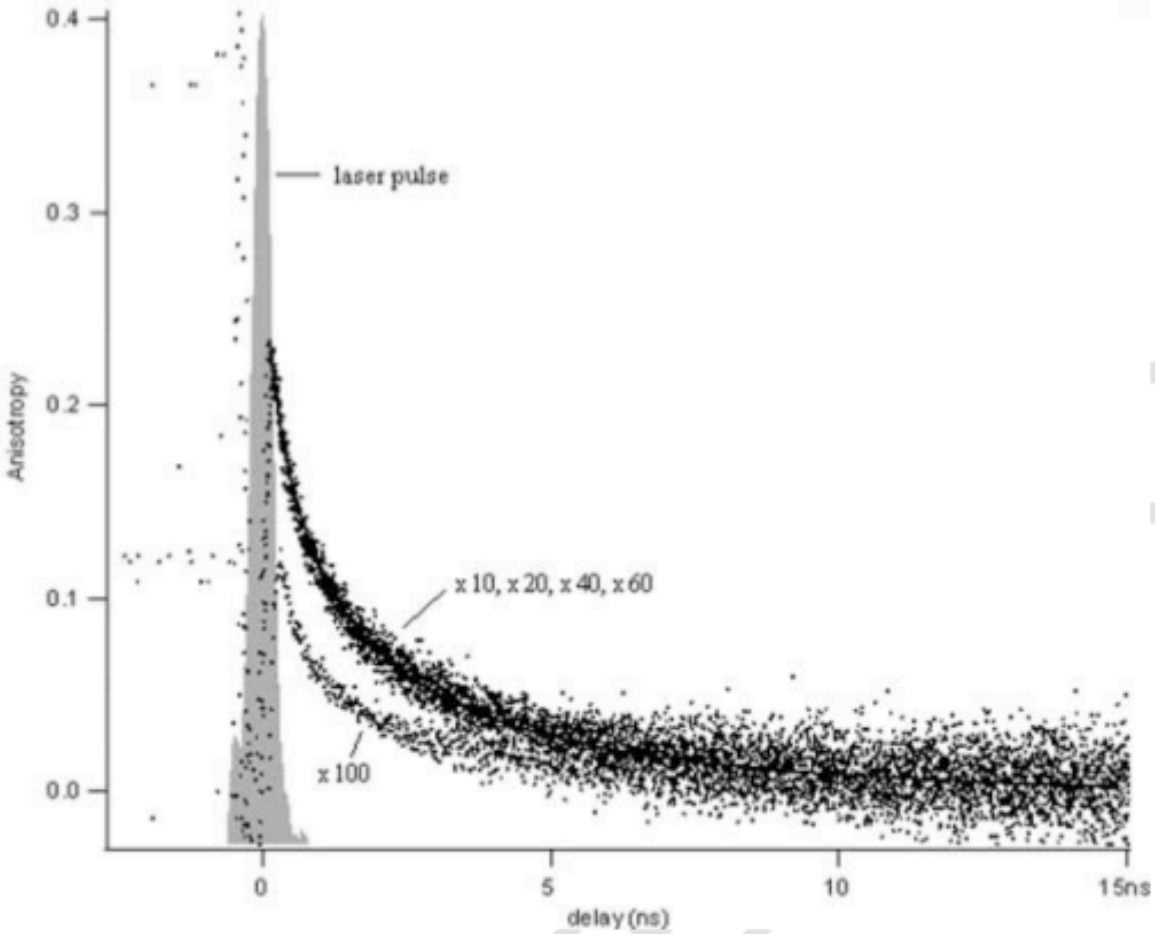

Figure 17 : Time-resolved anisotropy of PM567 in PMMA film with different numerical aperture. The anisotropy has been calculated according to Eq. (1)
from the decays recorded using five dif ferent microscope objectives. The laser pulse has been superimposed to the figure.

The angular distribution $\rho(\theta,\phi)$ of the transition dipole after one jump is given by averaging __ over $\vec{u}$. This average gives a distribution $\rho(\theta,\phi)=(3+\cos\_(\theta))$ which corresponds to a reduction of anisotropy down to a value of 4% of the original value (Agranovich et Galanin 1982). Some authors show that this is zero (Berberan-Santos et Valeur 1991). Thus the rate of the anisotropy relaxation is the rate of the energy transfer to the first neighbour

$$r(t) = r_0 \exp(-\sqrt{\frac{t}{\tau}})$$ (Förster 1959; Millar *et al.* 1981) (6).

Anisotropy decays have been fitted to this equation leading to the initial anisotropy (r_0) and the characteristic time of the energy transfer (_) gathered in Table 2. Apart from the highest numerical aperture, the anisotropy depolarization can also be neglected.

Conclusion

We describe a robust and useful set-up to measure fluorescence anisotropy imaging. The whole decay profile of the two polarizations is acquired simultaneously with a single photon counting system. Thus, there is no sampling of the fluorescence and the two polarizations are acquired at the same time, with the same sample, at the same position, with the same experimental conditions preventing us from artefacts such as instrument drift, evolution of the sample and photobleaching. Since FLIM can be estimated with a limited number of photons, FLIM images can be recorded with a single-photon counting system in less than one minute. Correction maps are required for gain and transit time. These correction maps appear to be stable for a few months and recalibration of the set-up is easy on a few reference samples. Overall, this device appears to be a powerful and sensible tool to do imaging in different fields such as cellular imaging (Fig. 18), chemical sensing, μTAS, biochip diagnostic…

References

Agranovich, V. M. et Galanin, M. D. (1982). Electronic Excitation Energy Transfer in Condensed Matter. Amsterdam, Elsevier.

Axelrod, D. (1979). "Carbocyanine dye orientation in red cell membrane studied by microscopic fluorescence polarization." Biophys J **26**(3): 557-73.

Berberan-Santos, M. N. et Valeur, B. (1991). "Fluorescence depolarization by electronic energy transfert in donor-acceptor pairs of like and unlike chromophores." J. Chem. Phys. **11**: 8048-8055.

Buurman, E. P., Sanders, R., Draaijer, A., Gerritsen, H. C., van Veen, J. J. F., Houpt, P. M. et Levine, Y. K. (1992). "Fluorescence lifetime imaging using a confocal laser scanning microscope." Scanning **14**: 155-159.

Clayton, A. H., Hanley, Q. S., Arndt-Jovin, D. J., Subramaniam, V. et Jovin, T. M. (2002). "Dynamic fluorescence anisotropy imaging microscopy in the frequency domain (rFLIM)." Biophys J **83**(3): 1631-49.

Emiliani, V., Sanvitto, D., Tramier, M., Piolot, T., Petrasek, Z., Kemnitz, K., Durieux, C. et Coppey-Moisan, M. (2003). "Low-intensity two-dimensional imaging of fluorescence lifetimes in living cells." Applied Physics Letters **83**(12): 2471-2473.

Enderlein, J. (2000). "Theoritical study of detecting a dipole emitter through an objective with high numerical aperture." Optics Letters **25**: 634-636.

Fleming, G. R. (1986). Chemical application of ultrafast spectroscopy, Oxford University press.

Förster, T. (1959). "Transfer mechanisms of electronic excitation." Disc.Faraday Soc **27**: 7-17.

Gadella, T. W. J., Jovin, T. M. et Clegg, R. M. (1993). "Fluorescence lifetime imaging microscopy (FLIM): Spatial resolution of microstructures on the nanosecond time scale." Biophys. Chem. **48**(1): 221-239.

Gautier, I., Tramier, M., Durieux, C., Coppey, J., Pansu, R. B., Nicolas, J. C., Kemnitz, K. et Coppey-Moisan, M. (2001). "Homo-FRET microscopy in living cells to measure monomer-dimer transition of GFP-tagged proteins." Biophys J **80**(6): 3000-8.

Ha, T., Laurence, T. A., Chemla, D. S. et Weiss, S. (1999). "Polarization spectroscopy of single fluorescent molecules." J. Phys. Chem. B **103**(33): 6839-6850.

Herman, B., Wang, X. F., Wodnicki, P., Perisamy, A., Mahajan, N., Berry, G. et Gordon, G. (1999). Fluorescence Lifetime Imaging Microscopy. Applied Fluorescence in Chemistry, Biology and Medecine. W. Rettig, B. Strehmel, S. Schrader and H. Seifert. Berlin, Springer.

Lakowicz, J. R. (1999). Principles of Fluorescence Spectroscopy. New York, Kulwer Academic/Plenum Publishers.

Magde, D., Wong, R. et Seybold, P. G. (2002). "Fluorescence quantum yields and their relation to lifetimes of rhodamine 6G and fluorescein in nine solvents: improved absolute standards for quantum yields." Photochem Photobiol **75**(4): 327-34.

Méallet-Renault, R., Yoshikawa, H., Tamaki, Y., Asahi, T., Pansu, R. B. et Masuhara, H. (2000). "Confocal microscopic study on fluorescence quenching of single latex beads in poly(vinyl alcohol) film." Polymer for Advanced Technologies **11**(8-12): 772-777.

Millar, D. P. (1996). "Time-resolved fluorescence spectroscopy." Curr Opin Struct Biol **6**(5): 637-42.

Millar, D. P., Robbins, R. J. et Zewail, A. H. (1981). "Picosecond dynamics of electronic energy transfer in condensed phases." J. Chem. Phys. **75**(8): 3649-59.

Miyawaki, A., Llopis, J., Heim, R., McCaffery, J. M., Adams, J. A., Ikura, M. et Tsien, R. Y. (1997). "Fluorescent indicators for Ca2+ based on green fluorescent proteins and calmodulin." Nature **388**(6645): 882-7.

Schaffer, J., Volkmer, A., Eggeling, C., Subramaniam, V., Striker, G. et Seidel, C. A. M. (1999). "Identification of single molecules in aqueous solution by time resolved fluorescence anisotropy." J. Phys. Chem. A **103**(3): 331-336.

Schoutteten, L., Denjean, P., Joliff-Botrel, G., Bernard, C., Pansu, D. et Pansu, R. B. (1999). "Development of intracellular calcium measurement by time-resolved photon-counting fluorescence." Photochem Photobiol **70**(5): 701-9.

Schoutteten, L., Denjean, P. et Pansu, R. B. (1997). "Characterisation of a Time resolved Photon Counting Confocal Fluorescence Microscope." Journal of Fluorescence **7**(2): 155-165.

Siegel, J., Suhling, K., Leveque-Fort, S., Webb, S. E. D., Davis, D. M., Phillips, D., Sabharwal, Y. et French, P. M. W. (2003). "Wide-field time-resolved fluorescence anisotropy imaging (TR-FAIM): Imaging the rotational mobility of a fluorophore." Review of Scientific Instruments **74**(1): 182-192.

So, P. T., French, T., Yu, W., Berland, K., Dong, C. Y. et Gratton, E. (1995). "Time-Resolved Fluorescence Microscopy Using Two-photon Excitation." Bioimaging **3**: 49-63.

So, P. T., Konig, K., Berland, K., Dong, C. Y., French, T., Buhler, C., Ragan, T. et Gratton, E. (1998). "New time-resolved techniques in two-photon microscopy." Cell Mol Biol (Noisy-le-grand) **44**(5): 771-93.

Tramier, M., Kemnitz, K., Durieux, C., Coppey, J., Denjean, P., Pansu, R. B. et Coppey-Moisan, M. (2000). "Restrained torsional dynamics of nuclear DNA in living proliferative mammalian cells." Biophys J **78**(5): 2614-27.

Tripathi, N. (2005). "Densities, Viscosities, and Refractive Indices of Mixtures of Hexane with Cyclohexane, Decane, Hexadecane, and Squalane at 298.15K." International Journal of Thermophysics **26**(3): 693-703.

Valeur, B. (2001). Molecular Fluorescence : Principle and Applications, Wiley.

Wang, X. F., Perisamy, A. et Herman, B. (1992). "Fluorescence Lifetime Imaging Microscopy (FLIM) : Instrumentation and Applications." Crit. Rev. Anal. Chem. **23**: 369-395.

Obj	N.A.	r_0	r_c	$\_{rot}$ (ns)
0	0	0.297	-	2.65
10	0.3	0.281	0.318	2.66
40	0.6	0.272	0.311	2.52
60	0.95	0.283	0.293	2.50
100	1.45	0.234	0.244	2.66

Table 1: Time zero anisotropy (r_0) of rubrene in squalane with different numerical aperture (NA); calculated anisotropy (r_C); rotational correlation time ($\_{rot}$)

Obj.	N.A.	r_0	r_C	_ (ps)
10	0.3	0.348	0.330	865
20	0.45	0.335	0.327	865
40	0.6	0.332	0.322	819
60	0.95	0.344	0.304	807
100	1.45	0.213	0.252	739

Table 2: Time zero anisotropy (r_0) of PM567 in PMMA films with different numerical aperture (NA and characteristic time of the energy transfer (_)

Figure captions

Fig. 1: Experimental setup.

Fig. 2: Optical pathway in the polarization separator

Fig. 3: Time transit correction. a) Crude image of rhodamine 6G in water sample. b) Time transit correction map. Determined with another sample of the same type. c) Corrected image of the first sample using the time transit correction map.

Fig. 4: Histogram of the collected photons vs. lifetime before and after correction of time transit

Fig. 5: Evolution of the lifetime dispersion with the number of photons per pixel. The pixels of an image of a rhodamine sample were sorted according to their intensity and the lifetime distribution was fitted with a Gaussian whose width is the lifetime dispersion.

Fig. 6: Pulse and corrected pulse.

Fig. 7: Gain correction. a) Crude image of a rhodamine in water sample. b) Gain factor correction map calculated from another sample. c) Corrected image of the first sample using the gain factor correction map.

Fig. 8: Position of the anodes on the detector surface.

Fig. 9: Determination of the dead time.

Fig. 10: Saturation curve.

Fig. 11: Images of spin-coated 20 nm fluorescent nanolatex in PVA film. b is the image in focal plane, a is the image 1.2 µm underneath and c is the image 5 µm over the focal plane.

Fig. 12: a) 2-D Gaussian fit of the fluorescent spot of a 20 nm fluorescent nanolatex. b) Gaussian's width vs. altitude.

Fig. 13: Parallel and perpendicular decays of rubrene fluorescence. Fluorescence decays of rubrene in solution in squalane, before correction of the pathway shift.

Fig. 14: FLIM image of the two polarization components of the fluorescence of rubrene in squalane.

Fig. 15: Fluorescence decays of rubrene in squalane. The decays have been recorded using 4 different microscope objectives and numerical apertures. The decay for parallel polarization (resp. perpendicular) has been calculated from the upper part (resp. bottom part) of the image.

Fig. 16: Time resolved anisotropy of rubrene in squalane with different numerical apertures. The anisotropy has been calculated according to the formula n°1 from the decays recorded using 4 different microscope objectives.

Fig.17: Time resolved anisotropy of PM567 in PMMA film with different numerical aperture. The anisotropy has been calculated according to the formula n°1 from the decays recorded using 5 different microscope objectives. The laser pulse has been superimposed to the figure.

Fig. 18: Intensity image of a NIH 3T3 cell. Actin cytoskeleton is stained with phalloïdine-Alexa.